Journal of Quantitative Spectroscopy & Radiative Transfer 262 (2021) 107527

Contents lists available at ScienceDirect

Journal of Quantitative Spectroscopy & Radiative Transfer

journal homepage: www.elsevier.com/locate/jqsrt

Near-infrared cavity ring-down spectroscopy measurements of nitrous oxide in the (4200)←(0000) and (5000)←(0000) bands

Erin M. Adkins*, David A. Long*, Adam J. Fleisher, Joseph T. Hodges

National Institute of Standards and Technology, Gaithersburg, MD 20899, USA

ARTICLE INFO

Article history:
Received 17 December 2020
Revised 15 January 2021
Accepted 17 January 2021
Available online 20 January 2021

Keywords:
Line lists
Nitrous oxide
Cavity ring-down spectroscopy

ABSTRACT

Using frequency-agile rapid scanning cavity ring-down spectroscopy, we measured line intensities and line shape parameters of $^{14}N_2{}^{16}O$ in air in the (4200)←(0000) and (5000)←(0000) bands near 1.6 μm. The absorption spectra were modeled with multi-spectrum fits of Voigt and speed-dependent Voigt profiles. The measured line intensities and air-broadening parameters exhibit deviations of several percent relative to values provided in HITRAN 2016. Our measured intensities for these two bands have relative combined standard uncertainties of ~1% which is approximately five times smaller than literature values. Comparison of the present air-broadening and speed-dependent broadening parameters to experimental literature values for other rotation-vibration bands of N_2O indicates significant differences in magnitude and *J*-dependence. For applications requiring high spectral fidelity, these results suggest that the assumption of band-independent line shape parameters is not appropriate.

Published by Elsevier Ltd.

1. Introduction

After carbon dioxide (CO_2) and methane (CH_4), nitrous oxide (N_2O) is the most important dry greenhouse gas with a 100-year global warming potential approximately 250 times that of CO_2 and 30 times that of CH_4 [1,2]. In 2015, the atmospheric background mole fraction of N_2O was 328 nmol/mol [1], which is increasing by 0.3% per year [2]. While microbial denitrification in both land and water are major natural sources of N_2O [3], industry, combustion, and agricultural sectors act as anthropogenic sources [1–4]. N_2O is removed from the atmosphere by relatively slow photolytic degradation, leading to an atmospheric lifetime greater than 100 years [3]. N_2O also plays a role in ozone depletion by acting as a major stratospheric source of nitrogen oxides [5]. Accurate measurements of N_2O concentration in the atmosphere and quantification of its sources and sinks are important to understanding the global nitrogen cycle [2], the role of anthropogenic contributions to this cycle, and accurate modeling of its radiative forcing.

Remote- and ground-based monitoring missions as well as point sensors require databases of spectroscopic parameters for N_2O and other target molecules in order to determine atmospheric concentrations. The High-Resolution Transmission (HITRAN) database provides a collection of high-resolution, line-by-line spectroscopic parameters for atmospherically relevant molecules across the electromagnetic spectrum that is formally updated on a quadrennial basis. Historically, HITRAN reports Voigt profile (VP) parameters, including collisional broadening parameters for both self- and air-broadening. The HITRAN 2004 update provided a large revision to the N_2O line list [6], which has not been substantially updated in later editions of HITRAN.

In 2004, Toth published an N_2O line list [7], based on the compilation of several Fourier-transform spectroscopy (FTS) studies [8–14] that spanned 500 cm^{-1} to 7500 cm^{-1}. In these works, the reported line frequencies and intensities were based on phenomenological band-wide models that were fit to the measured spectra, while collisional broadening and pressure shifting terms were modeled with empirical functions [8]. The line frequencies, intensities, air pressure shifts, and self-collisional broadening terms reported in HITRAN 2016 are derived from this Toth line list [15]. Between 2001 and 2007, Daumont et al. published several N_2O line intensity studies focused on fitting intensities measured by FTS to phenomenological band-wide models in 1.5 µm, 2.0 µm, and 10 µm regions [16–18].

At the time of the HITRAN 2004 update, in addition to the comprehensive work conducted by Toth, air broadening parameters had also been reported by Lacome et al. [19] and Nemtchinov et al. [20]. Both studies were based on FTS experiments conducted over a range of temperatures, where the Lacome et al. study measured the (2000)←(0000), (1200)←(0000), and (0200)←(0000) bands [19] and Nemtchinov et al. focused on the (0001)←(0000) band [20]. Both the HITRAN 2004 and the subsequent analysis reported in the high-temperature, nitrous-oxide spectroscopic data-

* Corresponding authors.
E-mail addresses: erin.adkins@nist.gov (E.M. Adkins), david.long@nist.gov (D.A. Long).

https://doi.org/10.1016/j.jqsrt.2021.107527
0022-4073/Published by Elsevier Ltd.

bank (NOSD) [21] gave only *J*-dependent collisional broadening terms for N_2O and notably did not specify any vibrational dependence to these parameters. Consequently, the air broadening terms reported for N_2O in HITRAN 2016 are based on a third-order polynomial fit (as a function of the rotational quantum number $|m|$) to the collisional broadening parameters reported in Toth [8], Lacome et al. [19], and Nemtchinov et al. [20]. This sole dependence on m was assumed despite the fact that these data corresponded to different rotation-vibration bands [6]. Also, we note that the average temperature exponent of 0.75 reported in Lacome et al. [19] and Nemtchinov et al. [20] was used as the temperature exponent for all N_2O transitions in HITRAN 2016.

In 2014, an IUPAC task group recommended a multi-parameter profile to model line shape effects which are not captured by the VP and are observable in high-resolution spectra [22]. The chosen profile, known as the Hartmann-Tran profile (HTP) [23] was selected to include relevant higher-order physical mechanisms, line-by-line parameterization, high computational speed, and the property that the HTP simplifies to other commonly used line profiles, including the VP [22]. In addition to the VP parameters (Doppler width, Γ_D, collisional broadening, γ_0, and pressure shifts, Δ_0), the HTP includes an additional four parameters: the rate of velocity-changing (VC) collisions or Dicke narrowing (ν_{vc}), the speed-dependence (SD) of the relaxation rates (speed-dependent broadening, γ_2, and speed-dependent shift, δ_2), and the correlation between the VC and SD mechanisms (η). The HTP simplifies to other commonly used line profiles by setting parameters to zero, such that the Nelkin-Ghatak profile (NGP) which accounts for Voigt parameters and Dicke narrowing, the speed-dependent Voigt profile (SDVP) which accounts for Voigt parameters and SD parameters, and the speed-dependent Nelkin-Ghatak profile (SD-NGP) which accounts for Voigt, SD, and VC parameters in the absence of correlation between SD and VC effects.

Based on the IUPAC recommendation and the needs of the high-resolution spectroscopy community, HITRAN 2016 extended the HITRAN database to include HTP parameters in addition to VP line-by-line parameters where the experimental data are available and validated [15]. This approach has greatly expanded the need for high-resolution spectroscopic reference data. Loos et al. measured the (0001)←(0000) fundamental band of N_2O in air with FTS and collected four spectra at pressures between 10 kPa and 100 kPa. These data were fit using the SDVP including Rosenkranz line mixing [24] and the reported air pressure-broadening, shifts, speed-dependence, and line-mixing were included in the HTP HITRAN 2016 parameters. Predoi-Cross et al. conducted a similar study in the same band using four N_2O-in-air spectra with pressures ranging from 15 kPa to 67 kPa. These spectra were also fitted with the SDVP and Rosenkranz line mixing, however the speed-dependent broadening term was constrained to theoretical values [25].

Because the studies of Loos et al. [24] and Predoi-Cross et al. [25] provide a comparison of N_2O advanced line profile parameters for the same band, they do not provide insight into the vibrational dependence of the line profile parameters. Liu et al. conducted comb-assisted cavity ring-down spectroscopy (CRDS) measurements of N_2O in nitrogen (N_2) in the (0003)←(0000) band near 1.52 μm. This study considered twenty isolated N_2O transitions [26] which were fit with the SDVP [26]. Using samples of pure N_2O, Odinstova et al. measured eight N_2O transitions in a combination of the (3200)←(0000), (0112)←(0000), and (3310)←(0110), bands near 2 μm using optical feedback laser absorption spectroscopy and reported line intensities and broadening parameters determined with the SDNGP and SDVP. Further, speed-dependent broadening and Dicke narrowing terms were determined with the SDNGP [27]. While the Liu et al. [26] and Odinstova et al. [27] studies provide valuable insights into the N_2- and self-broadening terms beyond the VP, the difference in broadeners makes it difficult to directly compare to the Loos et al. [24] and Predoi-Cross et al. [25] studies which were conducted in air.

Here we report measurements of 177 lines in the (4200)←(0000) and (5000)←(0000) rotation-vibration bands of $^{14}N_2{}^{16}O$ in air using frequency-agile rapid scanning cavity ring-down spectroscopy (FARS-CRDS). This study reports line intensities, as well as collisional broadening and speed-dependent broadening parameters determined by fits of the SDVP to measured spectra. Line intensities and collisional broadening terms were also determined using the VP model and are available in the Supplementary Materials. To the best of our knowledge, these are the first published line shape measurements for these near-infrared N_2O bands. The present line shape parameters also are compared to those in the current HITRAN 2016 N_2O line lists and provide insight into the vibrational dependence of these quantities.

2. Description of experiment

As the FARS-CRDS spectrometer employed in these measurements has previously been described in the literature [28–31], we will only briefly describe the method here. FARS-CRDS is a refinement of traditional CRDS in which an electro-optic phase modulator is employed to step a single selected laser sideband between successive modes of the optical cavity. This allows for spectra to be recorded at rates limited only by the cavity response time itself over ranges near 1 cm^{-1}. Full-band spectra are then recorded by stepping the external-cavity diode laser grating position. We note that for these measurements, we recorded a heterodyne beat signal between the probe laser and a Cs-clock-anchored, self-referenced optical frequency comb to provide an absolute frequency axis for each band-wide spectrum.

Measurements were made on static charges of N_2O-in-air provided by a gravimetric-based, primary gas standard mixture prepared at the National Institute of Standards and Technology (NIST). The standard mixture had an N_2O mole fraction of 0.57942% mol/mol and a standard uncertainty of 1.2×10^{-4}% mol/mol [32]. The nominal sample gas pressures were 9.3 kPa, 15.3 kPa, 29.1 kPa, 37.5 kPa, and 42.7 kPa (see Fig. 1 for typical spectra). The molecular composition of the diluting air in the primary gas mixture was measured to be 78.512(15)% mol/mol N_2, 20.852(8)% mol/mol O_2, 0.039(2)% mol/mol Ar, and 0.41(4) µmol/mol CO_2 [32]. The temperature of the sample cell varied between 296.66 K and 296.78 K over the course of the measurements. The pressure gage and thermistor were calibrated against NIST secondary standards.

The present measurements included five broadband spectra each containing more than 20,000 individual spectral points which must be fit in a multi-spectrum fashion to ensure the extraction of physically meaningful, uncorrelated spectroscopic parameters. Considering this need, we have recently developed the Multi-spectrum Analysis Tool for Spectroscopy (MATS). MATS is a Python fitting tool [33] that allows for experimental spectra to be fit with the HTP and its derivative line profiles through the use of the HITRAN application programming interface (HAPI) [34]. The Levenberg-Marquardt algorithm [35] is used to minimize the sum of the residuals between the modeled and experimental spectra. The fitted model incorporates a combination of background parameters that are unique to each input spectrum and includes spectroscopic parameters which are shared across all spectra in the dataset according to their pressure and temperature dependencies. MATS provides flexibility by allowing any spectroscopic parameter to be fit in either a single-spectrum or multi-spectrum fashion and for additional limits and constraints to be imposed on any given parameter. The ability to constrain parameter fits to their theoretical temperature and pressure dependences is critical to extracting physically meaningful and uncorrelated line shape parameters.

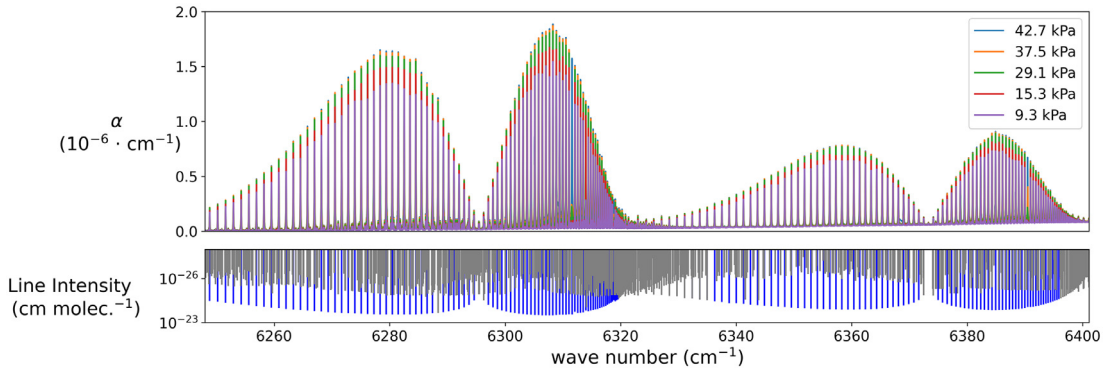

Fig. 1. (Top panel) Broadband N_2O FARS-CRDS spectra at selected pressures. (Bottom panel) To depict the high density of lines in the experimental spectral range, we present the line intensities of both the bands of interest (blue) as well as interfering lines (gray). These line intensities were obtained from single-spectrum fits of spectra acquired at a pressure of 9.33 kPa.

In the present experimental spectral range, HITRAN 2016 contains entries for the $^{14}N_2{}^{16}O$ (4200)←(0000) and (5000)←(0000) bands along with isolated $^{14}N_2{}^{18}O$ bands [(3400)←(0000), (3111)←(0000), and (3510)←(0110)]. The other N_2O isotopologues ($^{14}N^{15}N^{16}O$, $^{15}N^{14}N^{16}O$, and $^{14}N_2{}^{17}O$) and various $^{14}N_2{}^{16}O$ hot bands are not included in HITRAN 2016 for this region [15]. However, these transitions are above the noise floor of the experimental spectra and need to be included in the input spectroscopic line list. Several studies provide spectroscopic parameters that allow for the calculation of the line centers for the rare isotopologues and hot bands which are not in HITRAN 2016 [5,36–38]. However, in the absence of a robust model to constrain the intensities, the congested nature of the spectra and uncertainties in the computed line centers and experimental frequency axis made it difficult to incorporate these data into an initial line list. HITEMP provides a complete VP line list that includes a large number of hot bands for $^{14}N_2{}^{16}O$ in this region that are not included in HITRAN [39]. However, attempts to assign observed experimental peaks with the HITEMP line list, using band intensity, line center, and line intensity left approximately 20% of the observed lines unassigned. Because the focus of this study was the $^{14}N_2{}^{16}O$ (4200)←(0000) and (5000)←(0000) line profile parameters, unassigned interfering lines in the experimental spectra were identified and manually added to an initial line list comprising the HITRAN 2016 $^{14}N_2{}^{16}O$ (4200)←(0000) and (5000)←(0000) lines.

The lowest-pressure spectra and the initial HITRAN 2016 $^{14}N_2{}^{16}O$ (4200)←(0000) and (5000)←(0000) line lists were used as the inputs to MATS with only the baseline floated. Negative residuals with appropriate line widths were treated as lines missing from the input line list. These lines were subsequently added to the input line list with spectroscopic parameters initially set to match the adjacent lines and line intensities initially set to 10^{-25} cm molec.$^{-1}$. This updated line list was used to conduct a single-spectrum fit of the lowest-pressure spectrum with the baseline, line intensities, and line centers floated. These results were used to update the input spectroscopic line list to include the missing lines, which was then used for the multi-spectrum fitting. The HITRAN 2016 $^{14}N_2{}^{16}O$ (4200)←(0000) and (5000)←(0000) line list comprised 165 lines, but after this iterative process the resulting line list contained 924 lines. The only assignments of these lines that were attempted involved extending the $^{14}N_2{}^{16}O$ (4200)←(0000) and (5000)←(0000) assignments to higher J values, resulting in 177 reported lines.

To facilitate the fitting process, the measured spectra were separated into line-by-line spectra corresponding to wave number intervals of 1 cm^{-1} about each line in the $^{14}N_2{}^{16}O$ (4200)←(0000) and (5000)←(0000) bands. The optical cavity length was not stabilized during the data collection and the heterodyne beat signal measurement was made once per broadband scan, which increased the uncertainty in the frequency axis. In order to constrain the line centers across all pressures, it was necessary to float a frequency axis shift term to account for these small changes in the absolute frequency. Consequently, experimental line centers will not be reported, but tabulation of results will reference line centers reported by Toth [7]. Additionally, the spectra were collected on static samples of the N_2O, which can exhibit slight changes in the mole fraction of N_2O caused by adsorption and desorption from the optical cavity walls. To account for this complication, the line intensity was floated for each spectrum, while the mole fraction of N_2O was constrained to the reported sample value. This approach leads to an apparent variation in the line intensity derived from the fitted area and assumed N_2O mole fraction. We note that this statistical variation in fitted intensity was included in the line intensity uncertainty.

Because of the large number of studied transitions, we developed an automated fitting approach for each $^{14}N_2{}^{16}O$ line in the (4200)←(0000) and (5000)←(0000) bands. To this end, we analyzed the results by increasing the line profile complexity [VP, SDVP, NGP, SDNGP with a_w constrained to theory (i.e., SDNGP–a_w), and SDNGP with ν_{VC} (i.e., SDNGP–ν_{VC})] and using the theoretical values for a_w, where $a_w = \gamma_2/\gamma_0 = 0.06617$ [40], and $\nu_{VC} = 0.01788$ cm^{-1} atm^{-1} [41–43] as initial values. Fig. 2 depicts the fit of the (4200)←(0000) P20e line and the residuals from each of the line profiles. The residuals can depict apparent discontinuities due to laser grating tuning in the measurement collection. Additionally, the residuals in Fig. 2 near 6275.2 cm^{-1} highlight the difficulty in optimizing the spectroscopic parameters for small interfering lines located on the wings of transitions outside of the fit window. The quality of fit (QF), which is the ratio of the peak absorbance to the standard deviation of the fit residuals, increased with the use of line profiles more advanced than the VP. We found that the SDVP and the SDNGP–ν_{VC} tended to show higher QF values and smaller systematic residuals then the NGP and the SDNGP–a_w. We note that this is consistent with earlier N_2O line profile studies [24]. As a result, the VP and SDVP line lists will be reported, with the other advanced line profiles providing a measure of the line profile effects on the measured line intensity. The SDNGP with both narrowing parameters simultaneously floated had difficulties converging to meaningful physical values because of the limited signal-to-noise ratio. Additionally, the SDNGP–a_w and the SDNGP–ν_{VC} line lists are not reported as the choice and magnitude of the chosen constraint significantly affects the other parameters.

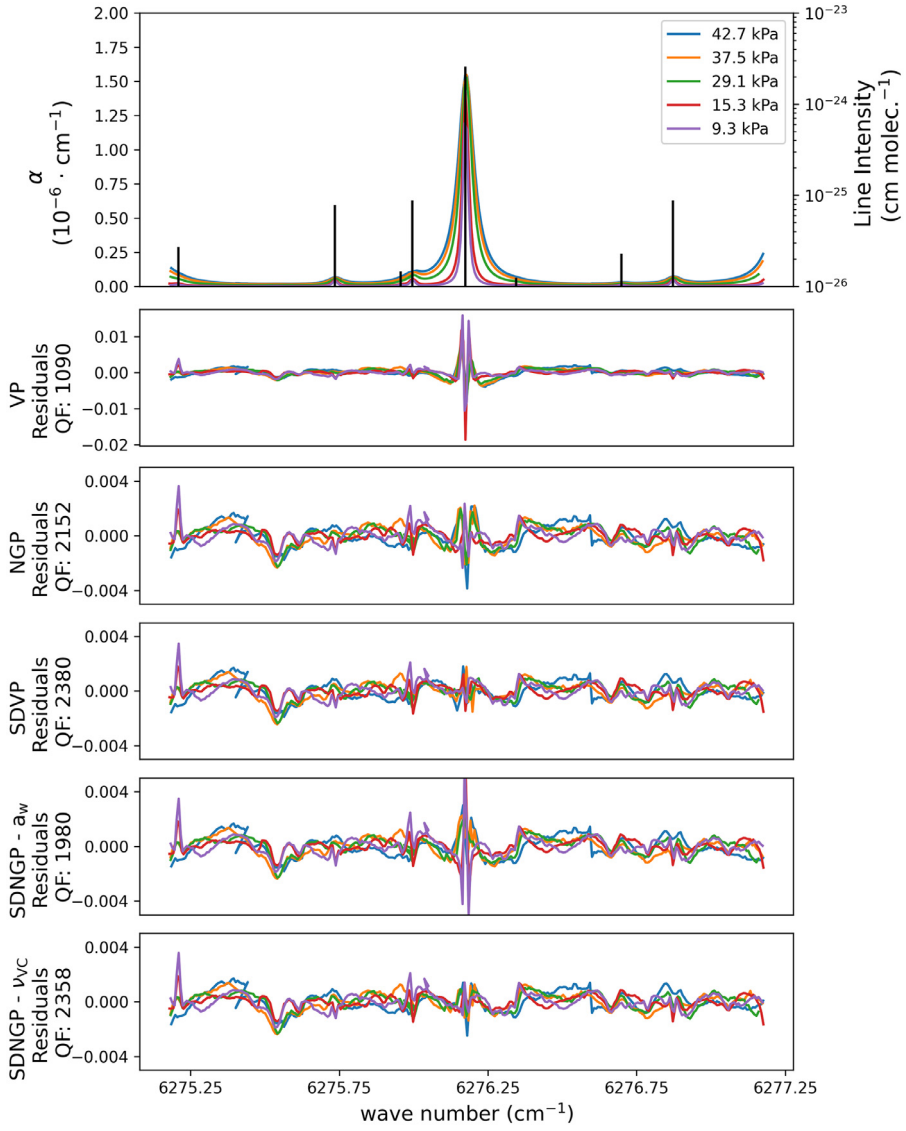

Fig. 2. (Top panel) Spectra centered on the (4200)←(0000) P20e transition. Secondary axis indicates the line intensity of all lines that were included in the fit of this spectral window (black lines). (Bottom panels) Fit residuals for VP, NGP, SDVP, SDNGP–a_w, and SDNGP–ν_{VC}. The QF averaged over the shown pressures is indicated for each line profile.

3. Results

FARS-CRDS was used to measure 177 lines in the (4200)←(0000) and (5000)←(0000) N_2O bands. The measured SDVP line intensities, collisional broadening parameters, and speed-dependent broadening parameters are reported in Tables 1 and 2 for the (4200)←(0000) and (5000)←(0000) N_2O bands, respectively. Analogous line lists for the VP are reported in the Supplementary Materials.

Line intensities

The final experimental line intensities, reported in Tables 1 and 2, are the weighted average across the five pressures with weighting factors $w_i = (1/\sigma_i^2)/\sum(1/\sigma_i^2)$, where $I_{296,i}$ / QF_i. The reported statistical (Type A) uncertainty for the line intensities is the quadrature sum of the standard deviation in the line intensity measured across the experimental pressures and the average fit uncertainty for each pressure. This relative uncertainty for the considered uncertainty is on average 0.95%.

The systematic (Type B) uncertainties in the line intensities are those associated with the pressure and temperature measurements, partition function, N_2O sample mole fraction, and choice of line profile. The estimated statistical and systematic uncertainties for the line intensities and other reported parameters are summarized in Table 3 and the combined standard uncertainty is tabulated in Tables 1 and 2. The pressure measurement has a 0.01% relative standard uncertainty, which propagates directly into the line intensity uncertainty. The temperature uncertainty affects the sample number density as well as the correction of the line intensity to the reference temperature (296 K). In addition to the uncertainty in the thermistor temperature reading of 20 mK, the uncertainty in the partition function affects the line intensity temperature correction. We took the magnitude of the −0.3380% relative difference between the TIPS-2011 and TIPS-2017 N_2O partition function values at 296 K as the uncertainty in the partition function [44]. We note that the relative abundances of the N_2O isotopologues in the gas sample were assumed to be consistent with those specified by HITRAN 2016, and consequently no corrections to the measured intensities were made.

Table 1
$^{14}N_2{}^{16}O$ (4200)←(0000) SDVP line list. Measured line shape parameters and corresponding combined standard uncertainties, represented by value in parentheses in units of last reported digit. Band model values for the line intensity are reported in addition to the Padé approximant smoothed values for the collisional broadening and speed-dependent parameters. The shown transition frequencies are from Ref. [7]. Units: ν_0 is given in cm^{-1}, S in 10^{-25} cm molec.$^{-1}$, γ_0^{air} in MHz Pa^{-1}, and a_w is dimensionless. Note that 1 cm^{-1} atm^{-1} = 0.29587215 MHz Pa^{-1}.

m	Line	ν_0	S		$\gamma_0{}^{air}$		a_w	
			Measured	Model	Measured	Smoothed	Measured	Smoothed
−42	P42e	6248.837736	3.27(4)	3.28(9)	0.02106(6)	0.02072(20)	0.076(8)	0.046(16)
−41	P41e	6250.221577	3.76(4)	3.79(10)	0.02091(4)	0.02079(21)	0.055(7)	0.049(17)
−40	P40e	6251.591935	4.30(4)	4.37(11)	0.02089(3)	0.02086(21)	0.058(4)	0.053(18)
−39	P39e	6252.948813	4.95(5)	5.01(12)	0.02093(3)	0.02094(21)	0.055(5)	0.056(19)
−38	P38e	6254.292216	5.73(5)	5.72(13)	0.02142(4)	0.02101(21)	0.087(5)	0.059(21)
−37	P37e	6255.622147	6.52(5)	6.49(14)	0.02151(4)	0.02109(21)	0.094(5)	0.062(22)
−36	P36e	6256.938614	7.29(7)	7.34(15)	0.02118(2)	0.02116(21)	0.065(3)	0.065(23)
−35	P35e	6258.241623	8.27(6)	8.26(16)	0.02162(3)	0.02125(21)	0.097(3)	0.068(24)
−34	P34e	6259.531182	9.26(7)	9.25(17)	0.02158(7)	0.02133(21)	0.092(8)	0.071(25)
−33	P33e	6260.807301	10.16(13)	10.30(17)	0.02117(2)	0.02141(21)	0.058(3)	0.074(26)
−32	P32e	6262.069988	11.41(8)	11.42(18)	0.02167(2)	0.02150(21)	0.090(3)	0.077(27)
−31	P31e	6263.319255	12.76(10)	12.60(19)	0.02161(2)	0.02159(21)	0.062(2)	0.079(28)
−30	P30e	6264.555112	13.78(11)	13.82(19)	0.02168(2)	0.02169(21)	0.080(2)	0.081(28)
−29	P29e	6265.77757	15.05(12)	15.09(20)	0.02175(1)	0.02179(22)	0.078(2)	0.084(29)
−28	P28e	6266.98664	16.35(14)	16.39(20)	0.02190(2)	0.02189(22)	0.085(2)	0.086(30)
−27	P27e	6268.182335	17.69(15)	17.71(21)	0.02198(1)	0.02199(22)	0.082(2)	0.087(30)
−26	P26e	6269.364665	19.03(16)	19.03(21)	0.02212(1)	0.02211(22)	0.088(2)	0.089(31)
−25	P25e	6270.533643	20.39(13)	20.33(21)	0.02241(2)	0.02222(22)	0.107(2)	0.091(31)
−24	P24e	6271.689282	21.66(13)	21.61(21)	0.02257(2)	0.02234(22)	0.108(2)	0.092(32)
−23	P23e	6272.831592	22.82(17)	22.83(21)	0.02253(1)	0.02247(22)	0.093(1)	0.093(32)
−22	P22e	6273.960586	23.90(19)	23.97(20)	0.02264(2)	0.02261(22)	0.096(2)	0.094(33)
−21	P21e	6275.076275	24.66(19)	25.03(20)	0.02282(2)	0.02276(22)	0.097(2)	0.094(33)
−20	P20e	6276.17867	25.88(21)	25.96(19)	0.02290(1)	0.02291(23)	0.092(1)	0.095(33)
−19	P19e	6277.267783	26.62(23)	26.75(19)	0.02304(1)	0.02308(23)	0.092(1)	0.095(33)
−18	P18e	6278.343623	27.22(24)	27.38(18)	0.02316(1)	0.02325(23)	0.088(1)	0.096(33)
−17	P17e	6279.406202	27.74(24)	27.83(17)	0.02349(1)	0.02344(23)	0.098(1)	0.096(33)
−16	P16e	6280.455528	28.08(20)	28.07(16)	0.02383(1)	0.02364(23)	0.100(1)	0.096(33)
−15	P15e	6281.491611	28.33(16)	28.09(16)	0.02433(2)	0.02386(24)	0.112(2)	0.095(33)
−14	P14e	6282.514458	27.71(25)	27.87(15)	0.02416(3)	0.02409(24)	0.094(4)	0.095(33)
−13	P13e	6283.524079	27.37(23)	27.41(14)	0.02453(2)	0.02434(24)	0.103(2)	0.095(33)
−12	P12e	6284.52048	27.76(23)	26.68(13)	0.02455(4)	0.02460(24)	0.094(4)	0.094(33)
−11	P11e	6285.503667	25.30(26)	25.69(12)	0.02468(3)	0.02488(25)	0.077(3)	0.094(33)
−10	P10e	6286.473645	24.36(19)	24.43(11)	0.02534(3)	0.02518(25)	0.101(3)	0.093(32)
−9	P9e	6287.430421	22.70(23)	22.91(10)	0.02538(2)	0.02548(25)	0.081(2)	0.092(32)
−8	P8e	6288.373997	21.62(19)	21.13(9)	0.02561(3)	0.02580(25)	0.058(3)	0.091(32)
−7	P7e	6289.304378	19.02(16)	19.11(7)	0.02613(4)	0.02612(26)	0.088(3)	0.090(31)
−6	P6e	6290.221565	16.74(15)	16.86(6)	0.02642(4)	0.02644(26)	0.085(4)	0.089(31)
−5	P5e	6291.125559	14.31(15)	14.41(5)	0.02671(3)	0.02678(26)	0.077(4)	0.088(31)
−4	P4e	6292.016361	11.74(11)	11.77(4)	0.02710(4)	0.02715(27)	0.072(4)	0.087(30)
−3	P3e	6292.893972	8.97(7)	8.98(3)	0.02769(5)	0.02757(27)	0.082(4)	0.086(30)
−2	P2e	6293.758388	5.97(8)	6.06(2)	0.02774(5)	0.02810(28)	0.049(6)	0.085(30)
−1	P1e	6294.609609	2.96(5)	3.06(1)	0.02898(11)	0.02887(28)	0.052(16)	0.084(29)
1	R0e	6296.272448	3.04(3)	3.08(1)	0.02901(8)	0.02887(28)	0.039(13)	0.084(29)
2	R1e	6297.084057	6.16(5)	6.13(2)	0.02870(6)	0.02810(28)	0.115(5)	0.085(30)
3	R2e	6297.882451	9.14(9)	9.14(3)	0.02768(3)	0.02757(27)	0.088(3)	0.086(30)
4	R3e	6298.667624	11.97(9)	12.05(5)	0.02721(4)	0.02715(27)	0.089(4)	0.087(30)
5	R4e	6299.439566	14.86(12)	14.83(6)	0.02691(8)	0.02678(26)	0.089(8)	0.088(31)
6	R5e	6300.19827	17.32(18)	17.46(7)	0.02629(3)	0.02644(26)	0.077(3)	0.089(31)
7	R6e	6300.943725	20.06(12)	19.90(8)	0.02645(2)	0.02612(26)	0.103(2)	0.090(31)
8	R7e	6301.675921	22.09(18)	22.13(10)	0.02576(2)	0.02580(25)	0.089(2)	0.091(32)
9	R8e	6302.394846	22.15(18)	24.13(11)	0.02581(3)	0.02548(25)	0.093(3)	0.092(32)
10	R9e	6303.100487	25.97(20)	25.89(12)	0.02531(3)	0.02518(25)	0.104(3)	0.093(32)
11	R10e	6303.792831	27.37(26)	27.38(13)	0.02479(4)	0.02488(25)	0.075(5)	0.094(33)
12	R11e	6304.471864	28.57(22)	28.60(15)	0.02455(1)	0.02460(24)	0.091(1)	0.094(33)
13	R12e	6305.137572	29.48(25)	29.56(16)	0.02439(2)	0.02434(24)	0.100(2)	0.095(33)
14	R13e	6305.789939	30.35(21)	30.24(17)	0.02433(3)	0.02409(24)	0.112(3)	0.095(33)
15	R14e	6306.428948	30.73(24)	30.66(19)	0.02382(2)	0.02386(24)	0.096(2)	0.095(33)
16	R15e	6307.054582	30.75(28)	30.82(20)	0.02346(4)	0.02364(23)	0.084(4)	0.096(33)
17	R16e	6307.666825	30.78(26)	30.73(21)	0.02350(2)	0.02344(23)	0.091(3)	0.096(33)
18	R17e	6308.265657	31.33(22)	30.42(22)	0.02340(3)	0.02325(23)	0.101(2)	0.096(33)
19	R18e	6308.851061	29.81(26)	29.91(23)	0.02294(2)	0.02308(23)	0.086(2)	0.095(33)
20	R19e	6309.423018	28.77(24)	29.20(24)	0.02285(2)	0.02291(23)	0.093(2)	0.095(33)
21	R20e	6309.981508	28.27(24)	28.32(25)	0.02262(2)	0.02276(22)	0.088(2)	0.094(33)
22	R21e	6310.526511	28.33(25)	27.30(26)	0.02253(2)	0.02261(22)	0.081(2)	0.094(33)
23	R22e	6311.058007	26.07(27)	26.15(26)	0.02220(9)	0.02247(22)	0.078(11)	0.093(32)
25	R24e	6312.080399	23.44(22)	23.59(27)	0.02197(3)	0.02222(22)	0.079(4)	0.091(31)
26	R25e	6312.571254	22.12(23)	22.22(27)	0.02182(9)	0.02211(22)	0.073(12)	0.089(31)
27	R26e	6313.048521	20.57(21)	20.81(27)	0.02158(2)	0.02199(22)	0.063(3)	0.087(30)

(*continued on next page*)

Table 1 (*continued*)

28	R27e	6313.512179	19.34(17)	19.38(27)	0.02171(4)	0.02189(22)	0.078(5)	0.086(30)
29	R28e	6313.962209	17.76(19)	17.96(26)	0.02177(3)	0.02179(22)	0.089(4)	0.084(29)
30	R29e	6314.398591	16.40(17)	16.56(26)	0.02143(3)	0.02169(21)	0.075(5)	0.081(28)
31	R30e	6314.821304	15.11(12)	15.19(25)	0.02143(3)	0.02159(21)	0.070(3)	0.079(28)
32	R31e	6315.23033	13.72(11)	13.86(24)	0.02141(3)	0.02150(21)	0.075(4)	0.077(27)
33	R32e	6315.62565	12.19(31)	12.59(23)	0.02063(3)	0.02141(21)	0.040(3)	0.074(26)
34	R33e	6316.007247	11.32(17)	11.37(22)	0.02130(4)	0.02133(21)	0.075(5)	0.071(25)
35	R34e	6316.375102	10.08(14)	10.23(21)	0.02102(4)	0.02125(21)	0.063(4)	0.068(24)
36	R35e	6316.729199	9.17(6)	9.16(20)	0.02151(3)	0.02116(21)	0.093(4)	0.065(23)
37	R36e	6317.069523	8.10(7)	8.15(19)	0.02140(3)	0.02109(21)	0.096(5)	0.062(22)
38	R37e	6317.396058	7.43(5)	7.23(18)	0.02105(4)	0.02101(21)	0.054(5)	0.059(21)
39	R38e	6317.708792	6.13(8)	6.38(17)	0.02062(4)	0.02094(21)	0.056(6)	0.056(19)
40	R39e	6318.007712	5.55(4)	5.60(15)	0.02118(11)	0.02086(21)	0.082(14)	0.053(18)
41	R40e	6318.292807	4.83(5)	4.90(14)	0.02107(13)	0.02079(21)	0.085(13)	0.049(17)
42	R41e	6318.564068	4.20(3)	4.26(13)	0.02115(10)	0.02072(20)	0.090(9)	0.046(16)
43	R42e	6318.821486	4.00(12)	3.69(12)	0.02096(11)	0.02065(20)	0.021(244)	0.043(15)
44	R43e	6319.065056	3.13(3)	3.19(11)	0.02062(8)	0.02059(20)	0.044(7)	0.040(14)
45	R44e	6319.294774	2.80(3)	2.74(10)	0.02216(13)	0.02052(20)	0.155(10)	0.037(13)
46	R45e	6319.510636	2.38(3)	2.34(9)	0.02185(27)	0.02045(20)	0.135(31)	0.033(12)
47	R46e	6319.712643	2.16(8)	1.99(8)	0.02328(38)	0.02039(20)	0.198(8)	0.030(11)
48	R47e	6319.900796	1.93(13)	1.69(7)	0.02414(46)	0.02033(20)	0.200(5)	0.028(10)
49	R48e	6320.075101	1.51(5)	1.42(6)	0.02231(37)	0.02027(20)	0.152(42)	0.025(9)
50	R49e	6320.235564	0.90(24)	1.19(5)	0.02627(126)	0.02021(20)	0.011(82)	0.022(8)
51	R50e	6320.382193	1.11(2)	1.00(5)	0.02299(50)	0.02015(20)	0.065(63)	0.019(7)

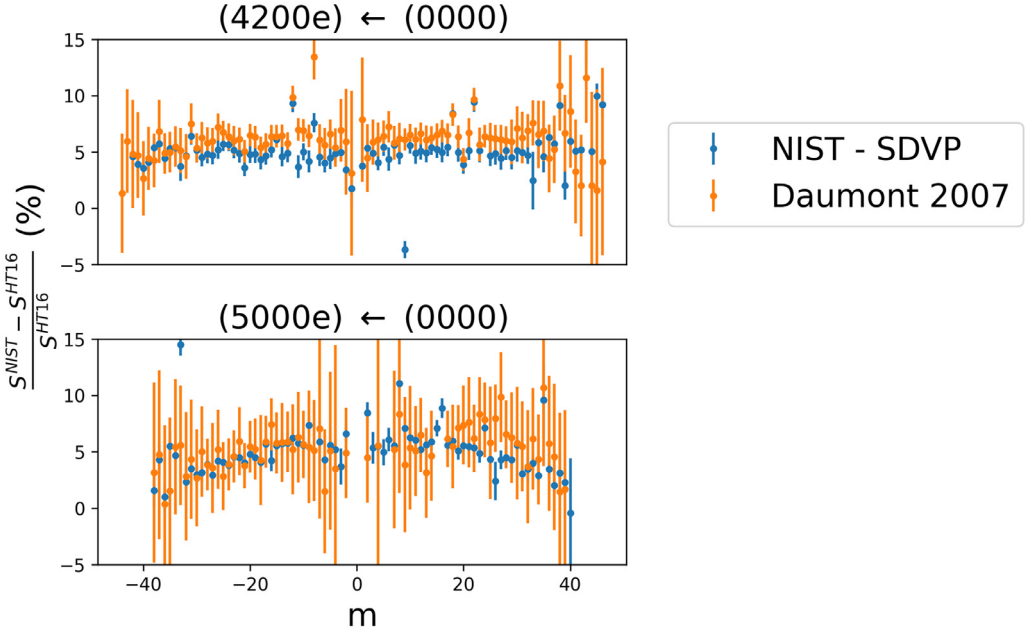

Fig. 3. Relative deviation of the experimentally determined SDVP line intensities and VP Daumont et al. [16] line intensities relative to HITRAN 2016 as a function of m.

To account for the line profile contribution to systematic uncertainty in fitted intensities, we evaluated the standard deviation in intensities based on use of the NGP, SDVP, SDNGP–a_w, and SDNGP-ν_{VC}. The VP was omitted from this line shape uncertainty quantification because the larger systematic residuals compared to the other line shapes lead to line intensities that are significantly biased. This analysis resulted in a 0.21% uncertainty component which is in good agreement with the 0.19% estimated by Odinstova et al. [27].

For the combined Type B evaluation of uncertainty in line intensity, we took the quadrature sum of the systematic components listed in Table 3, yielding a relative standard uncertainty of 0.21%, This uncertainty is dominated by the uncertainty associated with the choice of line profile. Adding the Type A and Type B contributions to the uncertainty in quadrature, the relative combined standard uncertainty for the intensities was nominally 1% for most lines.

Fig. 3 compares the present and the Daumont et al. [16] intensities with those in HITRAN 2016 [15] and illustrates that both the NIST and Daumont et al. intensities are roughly 5% greater across both bands. The Daumont et al. and NIST intensities show excellent agreement, with the Daumont et al. data being 0.97% larger in the (4200)←(0000) band and 0.07% larger in the (5000)←(0000) band. This is much less than the average uncertainty of 4.4% in the Daumont et al. line intensities [16]. The HITRAN 2016 line intensities are based upon the VP values reported by Toth and have relative uncertainties of 5% to 10% [7,15], which is roughly five to ten times greater than the present uncertainties. We note that only a small portion of the systematic difference between HITRAN 2016 and the present values can be ascribed to the choice in line profile, given that the average difference between the VP and SDVP line intensities reported in the present study was 0.7%. The Daumont et al. data also used the VP and resulted in line intensities that were larger than the present study.

Table 2
$^{14}N_2{}^{16}O$ (5000)←(0000) SDVP line list. Measured lineshape parameters and corresponding combined standard uncertainties, represented by value in parentheses in units of last reported digit. Band model values for the line intensity are reported in addition to the Padé approximant smoothed values for the collisional broadening and speed-dependent parameters. The shown transition frequencies are from Ref. [7]. Units: ν_0 is given in cm^{-1}, S in 10^{-25} cm molec.$^{-1}$, γ_0^{air} in MHz Pa^{-1}, and a_w is unitless. Note that 1 cm^{-1} atm^{-1} = 0.29587215 MHz Pa^{-1}.

m	Line	ν_0	S		$\gamma_0{}^{air}$		a_w	
			Measured	Model	Measured	Smoothed	Measured	Smoothed
−38	P38e	6332.387969	2.24(3)	2.22(7)	0.02106(8)	0.02101(21)	0.063(13)	0.059(21)
−37	P37e	6333.689111	2.64(4)	2.55(8)	0.02118(7)	0.02109(21)	0.051(12)	0.062(22)
−36	P36e	6334.979328	2.91(4)	2.91(8)	0.02107(7)	0.02116(21)	0.062(11)	0.065(23)
−35	P35e	6336.258481	3.44(5)	3.30(9)	0.02163(7)	0.02125(21)	0.057(10)	0.068(24)
−34	P34e	6337.526433	3.84(3)	3.73(9)	0.02177(6)	0.02133(21)	0.088(8)	0.071(25)
−33	P33e	6338.783057	4.71(5)	4.20(10)	0.02141(5)	0.02141(21)	0.063(7)	0.074(26)
−32	P32e	6340.028227	4.71(5)	4.70(10)	0.02141(5)	0.02150(21)	0.063(7)	0.077(27)
−31	P31e	6341.261825	5.26(4)	5.22(11)	0.02179(5)	0.02159(21)	0.074(7)	0.079(28)
−30	P30e	6342.483735	5.77(5)	5.78(11)	0.02176(3)	0.02169(21)	0.088(4)	0.081(28)
−29	P29e	6343.693848	6.37(6)	6.36(11)	0.02189(3)	0.02179(22)	0.092(4)	0.084(29)
−28	P28e	6344.892058	6.99(6)	6.96(12)	0.02211(4)	0.02189(22)	0.103(4)	0.086(30)
−27	P27e	6346.078265	7.52(8)	7.58(12)	0.02172(3)	0.02199(22)	0.051(5)	0.087(30)
−26	P26e	6347.252371	8.19(7)	8.20(12)	0.02220(3)	0.02211(22)	0.096(4)	0.089(31)
−25	P25e	6348.414286	8.81(7)	8.82(12)	0.02238(3)	0.02222(22)	0.101(3)	0.091(31)
−24	P24e	6349.56392	9.37(8)	9.44(12)	0.02236(3)	0.02234(22)	0.095(3)	0.092(32)
−23	P23e	6350.70119	9.99(7)	10.03(12)	0.02261(3)	0.02247(22)	0.102(3)	0.093(32)
−22	P22e	6351.826015	10.55(9)	10.60(12)	0.02262(3)	0.02261(22)	0.095(4)	0.094(33)
−21	P21e	6352.938321	11.03(10)	11.12(12)	0.02272(3)	0.02276(22)	0.088(4)	0.094(33)
−20	P20e	6354.038034	11.53(8)	11.60(11)	0.02302(3)	0.02291(23)	0.089(4)	0.095(33)
−19	P19e	6355.125086	11.91(9)	12.02(11)	0.02302(3)	0.02308(23)	0.090(3)	0.095(33)
−18	P18e	6356.199412	12.17(11)	12.36(10)	0.02312(2)	0.02325(23)	0.082(2)	0.096(33)
−17	P17e	6357.260952	12.58(8)	12.62(10)	0.02383(3)	0.02344(23)	0.110(3)	0.096(33)
−16	P16e	6358.309647	12.61(12)	12.78(10)	0.02340(3)	0.02364(23)	0.066(5)	0.096(33)
−15	P15e	6359.345443	12.77(10)	12.84(9)	0.02405(4)	0.02386(24)	0.105(5)	0.095(33)
−14	P14e	6360.368289	12.69(13)	12.79(8)	0.02418(14)	0.02409(24)	0.090(15)	0.095(33)
−13	P13e	6361.378139	12.59(13)	12.61(8)	0.02467(14)	0.02434(24)	0.076(17)	0.095(33)
−12	P12e	6362.374947	12.22(10)	12.32(7)	0.02488(14)	0.02460(24)	0.092(15)	0.094(33)
−11	P11e	6363.358674	11.74(8)	11.89(7)	0.02494(3)	0.02488(25)	0.087(3)	0.094(33)
−10	P10e	6364.329281	11.19(11)	11.34(6)	0.02520(3)	0.02518(25)	0.087(3)	0.093(32)
−9	P9e	6365.286733	10.69(8)	10.66(5)	0.02578(4)	0.02548(25)	0.106(4)	0.092(32)
−8	P8e	6366.231001	10.76(6)	9.85(5)	0.02608(6)	0.02580(25)	0.123(5)	0.091(32)
−7	P7e	6367.162054	8.84(8)	8.93(4)	0.02632(17)	0.02612(26)	0.087(19)	0.090(31)
−6	P6e	6368.079869	7.70(7)	7.89(4)	0.02622(5)	0.02644(26)	0.068(5)	0.089(31)
−5	P5e	6368.984422	6.64(9)	6.75(3)	0.02662(9)	0.02678(26)	0.066(11)	0.088(31)
−4	P4e	6369.875696	5.43(6)	5.52(2)	0.02702(13)	0.02715(27)	0.069(15)	0.087(30)
−3	P3e	6370.753673	4.07(7)	4.21(2)	0.02714(14)	0.02757(27)	0.056(16)	0.086(30)
−2	P2e	6371.618341	2.83(2)	2.85(1)	0.02846(20)	0.02810(28)	0.099(19)	0.085(30)
−1	P1e	6372.469689	1.42(2)	1.44(1)	0.02906(59)	0.02887(28)	0.074(52)	0.084(29)
1	R0e	6374.1324	1.38(4)	1.44(1)	0.02860(17)	0.02887(28)	0.034(32)	0.084(29)
2	R1e	6374.943758	2.91(3)	2.88(1)	0.02948(14)	0.02810(28)	0.148(10)	0.085(30)
3	R2e	6375.741786	4.20(6)	4.28(2)	0.02698(13)	0.02757(27)	0.022(22)	0.086(30)
4	R3e	6376.526487	5.53(5)	5.64(3)	0.02697(5)	0.02715(27)	0.071(5)	0.087(30)
5	R4e	6377.297871	6.77(8)	6.93(3)	0.02655(22)	0.02678(26)	0.052(31)	0.088(31)
6	R5e	6378.055947	8.04(8)	8.14(4)	0.02646(5)	0.02644(26)	0.086(4)	0.089(31)
7	R6e	6378.800729	9.11(11)	9.26(5)	0.02622(25)	0.02612(26)	0.054(32)	0.090(31)
8	R7e	6379.532233	10.66(11)	10.28(6)	0.02578(20)	0.02580(25)	0.068(25)	0.091(32)
9	R8e	6380.250481	11.14(10)	11.18(6)	0.02565(23)	0.02548(25)	0.106(23)	0.092(32)
10	R9e	6380.955494	11.90(9)	11.96(7)	0.02540(3)	0.02518(25)	0.106(3)	0.093(32)
11	R10e	6381.647299	12.51(11)	12.61(8)	0.02487(4)	0.02488(25)	0.090(4)	0.094(33)
12	R11e	6382.325924	12.94(10)	13.13(9)	0.02454(2)	0.02460(24)	0.096(2)	0.094(33)
13	R12e	6382.991403	13.42(11)	13.52(10)	0.02427(2)	0.02434(24)	0.093(3)	0.095(33)
14	R13e	6383.643771	13.66(10)	13.78(10)	0.02405(3)	0.02409(24)	0.092(3)	0.095(33)
15	R14e	6384.283066	14.03(11)	13.91(11)	0.02373(3)	0.02386(24)	0.072(3)	0.095(33)
16	R15e	6384.909332	14.27(13)	13.93(12)	0.02348(2)	0.02364(23)	0.074(2)	0.096(33)
17	R16e	6385.522614	13.73(13)	13.82(13)	0.02335(3)	0.02344(23)	0.091(3)	0.096(33)
18	R17e	6386.122961	13.56(12)	13.62(13)	0.02333(2)	0.02325(23)	0.102(2)	0.096(33)
19	R18e	6386.710425	13.24(11)	13.32(14)	0.02306(2)	0.02308(23)	0.096(2)	0.095(33)
20	R19e	6387.285064	12.88(11)	12.93(15)	0.02291(2)	0.02291(23)	0.097(2)	0.095(33)
21	R20e	6387.846937	12.45(11)	12.47(15)	0.02280(2)	0.02276(22)	0.101(2)	0.094(33)
22	R21e	6388.396109	11.91(10)	11.95(16)	0.02259(2)	0.02261(22)	0.101(2)	0.094(33)
23	R22e	6388.932645	11.32(10)	11.37(16)	0.02237(2)	0.02247(22)	0.092(2)	0.093(32)
24	R23e	6389.456619	10.93(8)	10.76(16)	0.02244(2)	0.02234(22)	0.092(3)	0.092(32)
25	R24e	6389.968106	10.06(10)	10.12(16)	0.02201(3)	0.02222(22)	0.087(3)	0.091(31)
26	R25e	6390.467184	9.25(16)	9.46(16)	0.02201(5)	0.02211(22)	0.079(7)	0.089(31)
27	R26e	6390.953939	8.79(8)	8.80(16)	0.02189(3)	0.02199(22)	0.084(3)	0.087(30)
28	R27e	6391.428457	8.13(8)	8.13(16)	0.02174(3)	0.02189(22)	0.076(4)	0.086(30)
29	R28e	6391.890832	7.49(6)	7.48(16)	0.02176(3)	0.02179(22)	0.086(4)	0.084(29)
30	R29e	6392.34116	6.94(5)	6.84(16)	0.02211(6)	0.02169(21)	0.119(5)	0.081(28)

(*continued on next page*)

Table 2 (*continued*)

31	R30e	6392.779543	6.19(5)	6.22(15)	0.02141(4)	0.02159(21)	0.070(5)	0.079(28)
32	R31e	6393.206086	5.63(6)	5.62(15)	0.02142(5)	0.02150(21)	0.075(6)	0.077(27)
33	R32e	6393.620902	5.08(4)	5.06(14)	0.02131(5)	0.02141(21)	0.064(7)	0.074(26)
34	R33e	6394.024105	4.53(2)	4.53(13)	0.02121(5)	0.02133(21)	0.065(7)	0.071(25)
35	R34e	6394.415816	4.30(14)	4.04(13)	0.02123(15)	0.02125(21)	0.044(16)	0.068(24)
36	R35e	6394.796163	3.60(3)	3.58(12)	0.02132(8)	0.02116(21)	0.079(10)	0.065(23)
37	R36e	6395.165276	3.14(2)	3.15(11)	0.02111(12)	0.02109(21)	0.072(13)	0.062(22)
38	R37e	6395.523292	2.79(5)	2.77(11)	0.02153(12)	0.02101(21)	0.106(14)	0.059(21)
39	R38e	6395.870353	2.42(3)	2.41(10)	0.02122(12)	0.02094(21)	0.087(16)	0.056(19)
40	R39e	6396.206609	2.05(10)	2.10(9)	0.02104(27)	0.02086(21)	0.104(33)	0.053(18)
41	R40e	6396.532212	1.85(3)	1.81(8)	0.02134(18)	0.02079(21)	0.098(21)	0.049(17)
42	R41e	6396.847324	1.58(1)	1.56(8)	0.02130(20)	0.02072(20)	0.107(23)	0.046(16)
43	R42e	6397.15211	1.40(2)	1.33(7)	0.02114(28)	0.02065(20)	0.087(30)	0.043(15)
44	R43e	6397.446743	1.11(2)	1.14(6)	0.02032(22)	0.02059(20)	0.048(68)	0.040(14)
45	R44e	6397.731401	0.96(2)	0.96(6)	0.02058(26)	0.02052(20)	0.064(44)	0.037(13)
46	R45e	6398.006272	0.86(1)	0.81(5)	0.02163(38)	0.02045(20)	0.113(43)	0.033(12)
47	R46e	6398.271548	0.76(6)	0.68(4)	0.02352(163)	0.02039(20)	0.200(7)	0.030(11)

Table 3
Line shape parameter uncertainty analysis.

Line shape parameter	Parameter	u_r (%)	Description
S_m	**Type A**	0.95	SDVP average fit uncertainty and spread of measured values.
γ_0	**Type A**	0.23	
a_w	**Type A**	9.6	
S_m	**Type B**		
	p	0.01	Pressure gage uncertainty.
	T	0.01	Temperature sensor and partition function uncertainty.
	χ	0.02	Uncertainty in mole fraction of N_2O gas sample.
	Line profile selection	0.21	Uncertainty in S_w caused by choice of line profile.
	Combined Type B	0.21	
γ_0	**Type B**		
	p	0.01	Pressure gage uncertainty.
	T	0.011	Temperature sensor uncertainty and static temperature exponent.
	Broadener	0.16	Assumption that self-broadening is negligible.
	Combined Type B	0.16	
a_w	**Type B**		
	p	0.01	Pressure gage uncertainty.
	T	0.1	Temperature sensor and temperature exponent uncertainty.
	Broadener	0.16	Assumption that self-component is negligible.
	Combined Type B	0.19	
	Combined Types A & B		SDVP average relative combined standard uncertainty.
	S_m	0.97	
	γ_0	0.28	
	a_w	9.6	

For the inclusion of the measured line intensities into databases, such as HITRAN, it is beneficial to fit a vibrational band model to the available experimental results to allow for extrapolation to higher J values. The use of a phenomenological model is also important for this study as the use of an empirical line list to account for transitions not in HITRAN 2016 may not adequately constrain interfering lines and lead to potential bias in isolated transitions. The spectroscopic model applied to these data was described in Section 5.1.1 of Ref. [45]. Briefly, the spectroscopic model for m-dependent transition intensities is:

$$S_m = \frac{S_V \chi_{\text{iso}}}{g\tilde{\nu}_0 Q_R(T) F_0} \tilde{\nu}_m L_m F_m \left[1 - \exp\left(-\frac{hc\tilde{\nu}_m}{kT}\right)\right] \exp\left(-\frac{hcE_m''}{kT}\right). \quad (1)$$

In the $\nu_1\nu_2 l\nu_3$ HITRAN notation, the (4200)←(0000) and (5000)←(0000) bands of N_2O have $l = 0$, $\Delta l = 0$, and $g = 1$. With a rotational symmetry factor of $\sigma = 1$, the rotational partition function for a linear molecule with distinguishable nuclei is:

$$Q_R(T) = \frac{1}{\sigma} \sum_{J=0}^{\infty} g_J \exp\left(-\frac{hcE_J''}{kT}\right), \quad (2)$$

where E_J'' are the lower-state rotational energies with degeneracies $g_J = 2J + 1$. Assuming the rotational constants from Toth [7] and a temperature of $T = T_{\text{ref}} = 296$ K, we calculate $Q_R(T_{\text{ref}}) = 491.5266$ (with the summation performed up to $J_{\max} = 110$). Band centers, $\tilde{\nu}_0$, were taken from Table 2 of Toth [7], and the normalization factor, F_0, was calculated from Eq. (8) of Fleurbaey et al. [45]. For the Herman-Wallis factors

$$F_m = \left(1 + a_1 m + a_2 m^2 + a_3 m^3\right)^2. \quad (3)$$

Along with the Herman-Wallis coefficients, a_i, the vibrational band intensity, S_V, was floated while fitting the spectroscopic model to experimentally measured values of S_m. With a HITRAN isotopologue abundance for $^{14}N_2{}^{16}O$ of $\chi_{iso} = 0.990333$ [15], the

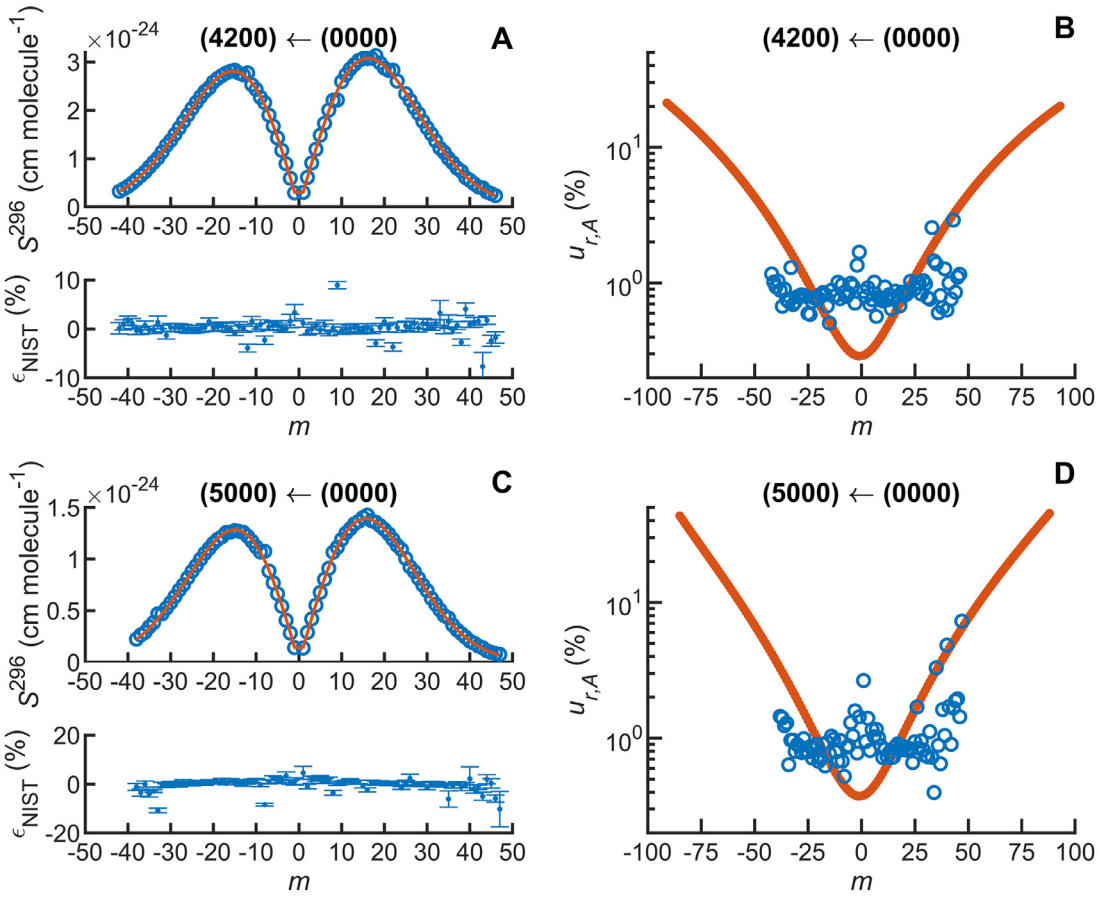

Fig. 4. Band-wide models for the present line intensities determined using the SDVP. (Panels A and C) Comparison of the experimental and band-wide model line intensities. (Panels B and D) Comparison of the Type-A-evaluated relative uncertainties in the experimental and band-wide intensity models for the bands of interest.

Table 4
Band-wide model parameters for the $^{14}N_2{}^{16}O$ (4200)←(0000) and (5000)←(0000) line intensities. The band center frequencies were taken from Ref. [7].

Parameter	Units	(4200)←(0000)	(5000)←(0000)
$\tilde{\nu}_0$	cm^{-1}	6295.4476	6373.3077
S^{446}_{band}	cm molec.$^{-1}$	$1.534(4) \times 10^{-22}$	$6.740(3) \times 10^{-23}$
a_1		$3.6(9) \times 10^{-4}$	$2.4(1.2) \times 10^{-4}$
a_2		$1.4(3) \times 10^{-5}$	$-5.2(4) \times 10^{-5}$
a_3		$8(13) \times 10^{-8}$	$8(19) \times 10^{-8}$
F_0		1.014948	0.950405
χ^2_ν		0.168	0.053
N		87	85

integrated band intensity was $S^{446}_{\text{band}} = \sum S_m = S_V \chi_{446,\text{HT}}$. When fitting Eq. (1) to the measured intensities, transition frequencies ($\tilde{\nu}_m$) and lower-state rotational energies (E''_m) calculated from Toth [7] were employed. Further, weighting factors for the vibrational band fits were assumed to be equal to the inverse of the variances in the measured values of S_m. The results from these band fits can be found in Table 4.

Panels (A) and (C) of Fig. 4 compare the experimental line intensities with the band-wide model. The model uncertainties are propagated as described in Section 5.2 of Ref. [45] and are added in quadrature to the line intensity Type-B-evaluated uncertainties reported in Table 3. The residuals in panels (A) and (C) highlight select lines where the difference between the band-wide model and the experimental line intensities are significantly larger than the experimental uncertainty. This indicates an unaccounted-for bias in the single line intensity measurement and highlights the advantages of modeling experimental data with band-wide phenomenological models. Panels (B) and (D) of Fig. 4 show the Type-A-evaluated uncertainties in the experimental line intensities compared to those propagated in the band-wide fit. These results illustrate the increase in the model uncertainties that occur with increasing $|m|$ and when extrapolating beyond the available data. We note that HITRAN 2016 reports relative uncertainties in the line intensities of the (4200)←(0000) and (5000)←(0000) N_2O bands between 5% and 10%, whereas the line intensities modeled in the present band-wide fits have relative combined uncertainties between 0.4% and 2% over the same range of m.

Collisional broadening parameter

We measured the collisional broadening parameter, γ_0, and the normalized speed-dependent broadening parameter, a_w, based upon SDVP fits to the measured spectra. These parameters along with the combined relative uncertainties are tabulated in Tables 1 and 2. Table 3 summarizes the average statistical uncertainties for each reported parameter and summarizes the contributions to the systematic uncertainties.

The statistical uncertainties in γ_0 for each line are taken from the standard error reported by the fit, whereas the systematic uncertainties in γ_0 are due to the pressure, temperature, and treatment of the self-broadening correction. The impact of the temperature uncertainty on γ_0 is based on the uncertainty in the thermistor reading and the use of a single temperature exponent for γ_0 for all lines reported in HITRAN 2016 and the present study. The average difference of the temperature exponents reported by

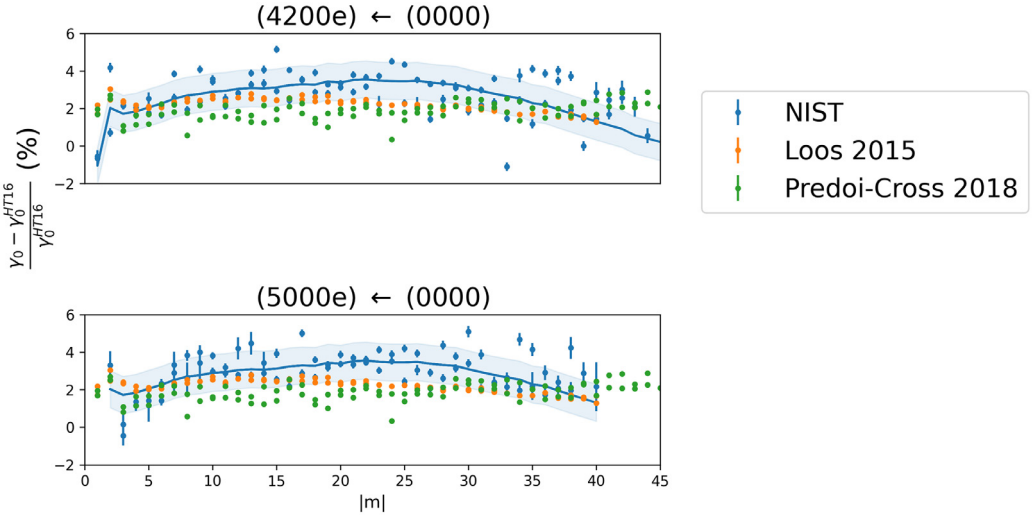

Fig. 5. Relative deviation between experimental SDVP air-broadening parameters (i.e., the present measurements, Loos et al. [24], and Predoi-Cross et al. [25]) and HITRAN 2016 as a function of |m|. The solid lines show the smoothed NIST air-broadening parameters while the shaded areas indicate corresponding uncertainty in the smoothing function.

Table 5
Fitted coefficients for the $|m|$-dependent band-wide Padé approximant equations (Eq. (4)) for γ_0 and a_w, respectively. These results are from fits to γ_0 and a_w values in the $^{14}N_2{}^{16}O$ (4200)←(0000) and (5000)←(0000) bands derived from measured spectra with the SDVP. γ_0 is in MHz Pa^{-1} and a_w is dimensionless. The Padé approximant uncertainty is defined by the relative standard deviation from the experimental values and is 0.97% for γ_0 and 35% for a_w. Note that 1 cm^{-1} atm^{-1} = 0.29587215 MHz Pa^{-1}.

Parameter	γ_0	a_w
c_0	0.03013	0.08318
c_1	0.006213	−0.00139
c_2	-1.752×10^{-4}	0
c_3	5.157×10^{-5}	0
d_1	0.2616	−0.02981
d_2	−0.009344	4.506×10^{-4}
d_3	2.274×10^{-3}	0
d_4	6.292×10^{-6}	0

Nemtchinov et al. and Lacome et al. [19,20] from those reported in HITRAN 2016 provides a measure of the uncertainty in the temperature exponent. Combining the thermistor and temperature exponent uncertainties led to a systematic relative uncertainty of 0.011% in γ_0. Because the mole fraction of the N_2O in the gas sample was nominally 0.5%, the self-broadening component was neglected in the present study. Based on the HITRAN 2016 self- and air-broadening terms, the magnitude of the neglected self-broadening component in this study was estimated to be 0.16%. A 3rd/4th order Padé approximant (Eq. (4)) was used to smooth the present experimental data, where p is the parameter and other parameters are smoothing coefficients. Both bands were used in a single weighted fit, resulting in residuals with a relative standard deviation of 0.97%. We use this quantity to estimate the standard uncertainty in the Padé approximant, which is represented by the shaded regions in Fig. 5. The Padé approximant coefficients are summarized in Table 5 with the smoothed values provided in Tables 1 and 2.

$$p = \frac{c_0 + c_1|m| + c_2|m|^2 + c_3|m|^3}{1 + d_1|m| + d_2|m|^2 + d_3|m|^3 + d_4|m|^4} \quad (4)$$

Fig. 5 compares the γ_0 values of the present study to those reported by the infrared FTS studies of Loos et al. [24] and Predoi-Cross et al. as well as to the air-broadening values from HITRAN 2016. The plotted FTS measurements were both conducted in the (0001)←(0000) band over a wide range of pressures (where line mixing needed to be included), whereas the present study was conducted at lower pressures where there was no evidence of line mixing. The two FTS measurements of γ_0 are in good agreement with one another with a weighted mean relative difference of 0.21%. However, the measured γ_0 values of the present study are on average 0.57% and 1.1% larger than those of Loos et al. [24] and Predoi-Cross et al. [25], respectively. Also, the present γ_0 results exhibit a stronger m-dependence relative to the HITRAN 2016 values unlike the FTS data which have a flatter m-dependence. Given the differences between the spectroscopic models (i.e., SDVP vs. SDVP with line mixing), measurement techniques, and the spectroscopic bands, further measurements would be useful to explain the reasons for these discrepancies.

In VP fits to spectra that exhibit line narrowing, fitted broadening coefficients are artificially reduced because they tend to compensate for this line shape effect which is not parameterized or captured by the VP. We found that γ_0 values determined with VP fits (not shown) were significantly smaller than those based on fits of more advanced line profiles. For the present study, γ_0 values determined with the SDVP were on average 1.9% larger than those with the VP. Predoi-Cross et al. reported a 1% increase for the same comparison [25].

Speed-dependent broadening parameter

The combined uncertainty of a_w can be estimated by adding in quadrature the standard error reported by the fit with the systematic uncertainties due to pressure, temperature, and broadener impacts (see Table 3). The uncertainty in gas pressure is assumed to be equal to the measurement uncertainty of the calibrated pressure gage. The temperature uncertainty contributions include the measurement of cell temperature and uncertainty in the temperature dependence of a_w. The theoretical expression for a_w given by Ghysels et al. [40] is temperature independent, with the collisional broadening term and the speed-dependent broadening term sharing a temperature dependence [40]. However, in the CO_2 FTS line shape study of Wilzewski et al. [46], γ_0 and γ_2 were found to have different temperature dependences, and consequently temperature exponents for both parameters were reported. Using CO_2 as an analogue, the difference between these values can be used as an estimate of the uncertainty on the temperature exponent of the speed-dependent broadening imposed using the collisional broad-

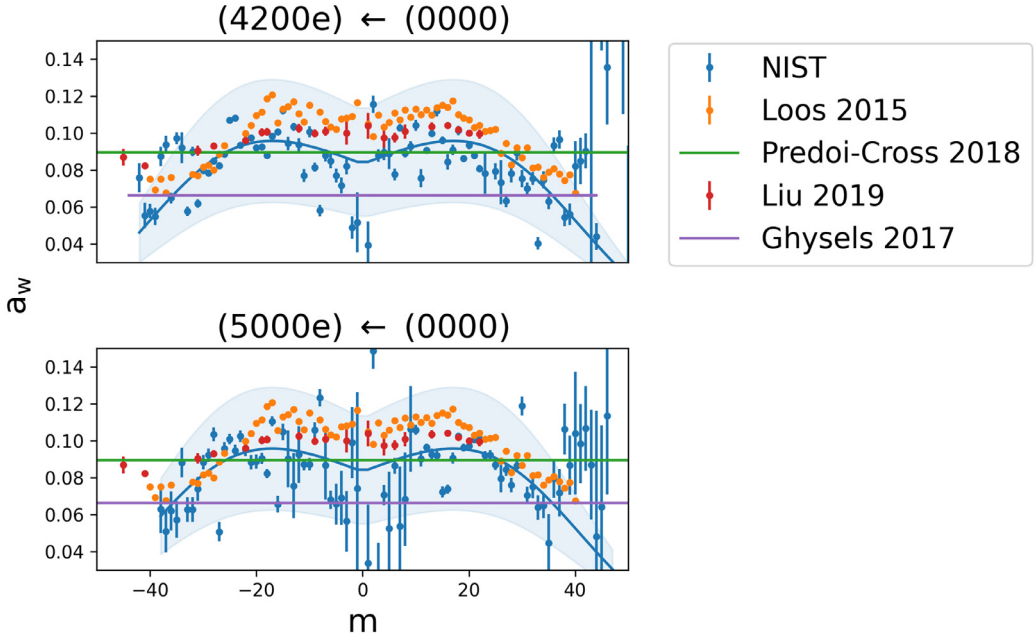

Fig. 6. Speed-dependent broadening terms for the present SDVP fits as well as the values from Loos et al. [24], Predoi-Cross et al. [25], Liu et al. [26], and theoretical a_w value calculated from Ghysels et al. based on $n = 0.75$ [40]. The blue solid line represents smoothed a_w data and the shaded areas indicate uncertainty of the smoothed data.

ening temperature exponent. This leads to a relative standard uncertainty of 0.1% in the speed-dependent broadening due to temperature. Like the collisional broadening, no attempt was made to separate the air- and self-contributions to a_w. The associated systematic uncertainty can be estimated by the difference between the theoretical a_w values for N_2O and air.

Fig. 6 compares the SDVP a_w terms from the present study with the values reported by Loos et al. [24], Predoi-Cross et al. [25], and Liu et al. [26]. We note that Liu et al. reported N_2-broadened N_2O measurements recorded with comb-assisted, CRDS near 1.52 μm. Although the results of Liu et al. were omitted from the collisional broadening discussion because of large differences between the air- and N_2-broadening parameters, we include their a_w measurements in this comparison. Based on the theoretical expression for the a_w given by Ghysels et al. [40], the N_2-induced value of speed-dependent narrowing should be approximately 2% less than the corresponding air-induced value: a difference that is smaller than the average measurement uncertainty of a_w in the present study. The $|m|$ dependence of the present speed-dependent narrowing parameters was smoothed with a 1st/2nd order Padé approximant (Eq. (4)). This empirical fit gives residuals with a relative standard deviation of 35% with which we estimate the uncertainty in the Padé approximant represented by the shaded regions in Fig. 6. The Padé approximant coefficients are summarized in Table 5 with the smoothed values provided in Tables 1 and 2.

Fig. 6 also shows the theoretical value of a_w calculated from Ghysels et al. [40] using the HITRAN 2016 temperature exponent of 0.75. In the Predoi-Cross et al. measurements a_w was not determined experimentally because of the limited spectrum signal-to-noise ratio. As a result, the values were constrained to the theoretical value given by Kochanov [47]. For N_2O in air, the Kochanov theoretical value of $a_w = 0.0895$ provides better agreement with the measured values than the theoretical value of Ghysels et al. of $a_w = 0.06617$ [40]. However, neither of these theoretical approximations for a_w capture the observed J-dependence.

The a_w terms reported in this study are lower than the Loos et al. [24] and Liu et al. values [26] by 14.7% and 3.4%, respectively. Also, the present results exhibit a much sharper decrease in a_w at low J'' than the earlier measurements. For both the collisional broadening and speed-dependent broadening terms, new physical models capturing the expected J-dependence of these parameters would provide useful constraints and tests for line shape studies, especially for experiments where the spectrum signal-to-noise ratio may be too low to precisely extract these parameters.

Conclusions

We report measurements of 177 lines in the (4200)←(0000) and (5000)←(0000) bands of $^{14}N_2{}^{16}O$ in air using frequency-agile rapid scanning, cavity ring-down spectroscopy. The reported line intensities have relative uncertainties at the 1% level and are at least five times lower than those available in HITRAN 2016. Further, the air-broadened line shape parameters exhibit deviations of several percent from the values available in HITRAN 2016. The differences between the air-broadening and speed-dependent Voigt parameters measured here and those available in the literature indicate the need for additional high-precision measurements of γ_0 and a_w for air-broadened N_2O. First-principles models for the J-dependencies of these quantities are also required to better understand observed band-to-band differences and to provide physical constraints for spectroscopic analyses.

Declaration of Competing Interest

The authors declare no competing interests.

CRediT authorship contribution statement

Erin M. Adkins: Writing - original draft, Writing - review & editing, Visualization, Software, Formal analysis, Data curation. **David A. Long:** Conceptualization, Investigation, Methodology, Writing - original draft, Writing - review & editing. **Adam J. Fleisher:** Writing - original draft, Writing - review & editing, Visualization, Formal analysis. **Joseph T. Hodges:** Conceptualization, Supervision, Project administration, Funding acquisition, Writing - review & editing.

Acknowledgements

We acknowledge funding from the NIST Greenhouse Gas and Climate Science Program and from the National Aeronautics and Space Administration (NASA) [contract NRA NNH17ZDA001N–OCO2].

Supplementary materials

Supplementary material associated with this article can be found, in the online version, at doi:10.1016/j.jqsrt.2021.107527.

References

[1] Climate change indicators in the united states. 4 ed. U.S. Environmental Protection Agency; 2016.
[2] Syakila A, Kroeze C. The global nitrous oxide budget revisited. Greenhouse Gas Meas Manage 2011;1:17–26.
[3] vanLoon GW, Duffy SJ. Environmental chemistry: a global perspective. Oxford: OUP; 2011.
[4] Parkes AM, Linsley AR, Orr-Ewing AJ. Absorption cross-sections and pressure broadening of rotational lines in the $3\nu_3$ band of N_2O determined by diode laser cavity ring-down spectroscopy. Chem Phys Lett 2003;377:439–44.
[5] Song KF, Gao B, Liu AW, Perevalov VI, Tashkun SA, Hu SM. Cavity ring-down spectroscopy of the bands of ^{15}N substituted N_2O. J Quant Spectrosc Radiat Transfer 2010;111:2370–81.
[6] Rothman LS, Jacquemart D, Barbe A, Benner DC, Birk M, Brown L, et al. The HITRAN 2004 molecular spectroscopic database. J Quant Spectrosc Radiat Transfer 2005;96:139–204.
[7] Toth RA. Linelist of N_2O parameters from 500 to 7500 cm^{-1}. JPL Online 2004.
[8] Toth RA. N_2- and air-broadened linewidth and frequency shifts of N_2O. J Quant Spectrosc Radiat Transfer 2000;66:285–304.
[9] Toth RA. Line Positions and Strengths of N_2O between 3515 and 7800cm^{-1}. J Mol Spectrosc 1999;197:158–87.
[10] Toth RA. Line strengths (900 -3600cm^{-1}), self-broadened linewidths, and frequency shifts (1800-2360cm^{-1}) of N_2O. Appl Opt 1993;32:7326–65.
[11] Benner DC, Blake TA, Brown LR, Malathy Devi V, Smith MAH, Toth RA. Air-broadening parameters in the ν_3 band of $^{14}N^{16}O_2$ using a multispectrum fitting technique. J Mol Spectrosc 2004;228:593–619.
[12] Toth RA. Frequencies of N_2O in the 1100- to 1440-cm^{-1} region. J Opt Soc Am B 1986;3:1263–81.
[13] Toth RA. N_2O vibration-rotation parameters derived from measurement in the 900-1090- and 1580-2380cm^{-1} regions. J Opt Soc Am B 1987;4:357–74.
[14] Toth RA. Line-Frequency measurements and analysis of N_2O between 900 and 4700cm^{-1}. Appl Optica 1991;30:5289–315.
[15] Gordon I.E., Rothman L.S., Hill C., Kochanov R.V., Tan Y., Bernath P.F., et al. The HITRAN2016 molecular spectroscopic database. 2017;203:3–69.
[16] Daumont L, Vander Auwera J, Teffo J-L, Perevalov VI, Tashkun SA. Line intensity measurements in $^{14}N_2{}^{16}O$ and their treatment using the effective dipole moment approach.II. The 5400–11000cm^{-1} region. J Quant Spectrosc Radiat Transfer 2007;104:342–56.
[17] Daumont L, Claveau C, Debacker-Barilly M-R, AHamdouni LRegalia-Jarlot, Teffo J-L, et al. LIne intensities of $^{14}N_2{}^{16}O$: the 10 micrometers region revisited. J Quant Spectrosc Radiat Transfer 2002;72:37–55.
[18] Daumont L, Auwera JV, Teffo JL, Perevalov VI, Tashkun SA. Line intensity measurements in $^{14}N_2{}^{16}O$ and their treatment using the effective dipole moment approach. J Mol Spectrosc 2001;208:281–91.
[19] Lacome N, Levy A, Guelachvili G. Fourier transform measurement of self-, N_2-, and O_2-broadening of N_2O lines: temperature dependence of linewidths. Appl Opt 1984;23:425–35.
[20] Nemtchinov V, Sun C, Varanasi P. Measurements of line intensities and line widths in the ν_3-fundamental band of nitrous oxide at atmospheric temperatures. J Quant Spectrosc Radiat Transfer 2004;83:267–84.
[21] Tashkun SA, Perevalov VI, Lavrentieva NN. NOSD-1000, the high-temperature nitrous oxide spectroscopic databank. J Quant Spectrosc Radiat Transfer 2016;177:43–8.
[22] Tennyson J, Bernath PF, Campargue A, Császár AG, Daumont L, Gamache RR, et al. Recommended isolated-line profile for representing high-resolution spectroscopic transitions (IUPAC Technical Report). Pure Appl Chem 2014;86:1931–43.
[23] Ngo N, Lisak D, Tran H, Hartmann J-M. An isolated line-shape model to go beyond the Voigt profile in spectroscopic databases and radiative transfer codes. J Quant Spectrosc Radiat Transfer 2013;129:89–100.
[24] Loos J, Birk M, Wagner G. Pressure broadening, -shift, speed dependence and line mixing in the ν_3 rovibrational band of N_2O. J Quant Spectrosc Radiat Transfer 2015;151:300–9.
[25] Predoi-Cross A, Hashemi R, Devi VM, Naseri H, Smith MAH. Analysis of Fourier transform spectra of N_2O in the ν_3 band for atmospheric composition retrievals. Can J Phys 2018;96:454–64.
[26] Liu GL, Wang J, Tan Y, Kang P, Bi Z, Liu AW, et al. Line positions and N_2-induced line parameters of the 00°3–00°0 band of $^{14}N_2{}^{16}O$ by comb-assisted cavity ring-down spectroscopy. J Quant Spectrosc Radiat Transfer 2019;229:17–22.
[27] Odintsova TA, Fasci E, Gravina S, Gianfrani L, Castrillo A. Optical feedback laser absorption spectroscopy of N_2O at 2μm. J Quant Spectrosc Radiat Transfer 2020;254:107190.
[28] Long DA, Truong G-W, van Zee RD, Plusquellic DF, Hodges JT. Frequency-agile, rapid scanning spectroscopy: absorption sensitivity of 2×10^{-12} cm^{-1} $Hz^{-1/2}$ with a tunable diode laser. Appl Phys B 2014;114:489–95.
[29] Long DA, Wójtewicz S, Miller CE, Hodges JT. Frequency-agile, rapid scanning cavity ring-down spectroscopy (FARS-CRDS) measurements of the (30012)←(00001) near-infrared carbon dioxide band. J Quant Spectrosc Radiat Transfer 2015;161:35–40.
[30] Reed ZD, Long DA, Fleurbaey H, Hodges JT. SI-traceable molecular transition frequency measurements at the 10^{-12} relative uncertainty level. Optica 2020;7:1209–20.
[31] Fleisher AJ, Adkins EM, Reed ZD, Yi H, Long DA, Fleurbaey HM, et al. Twenty–five-fold reduction in measurement uncertainty for a molecular line intensity. Phys Rev Lett 2019;123:043001.
[32] Kelley ME. Report of analysis: five level 2 gravimetric primary standard gas mixtures (0.5 - 0.7)% mol/mol prepared for analysis of nist N_2O in air standards. Gaithersburg: National Institute of Standards and Technology; 2011.
[33] Adkins EM. Multi-spectrum analysis tool for spectroscopy (MATS); 2020. doi:1018434/M32200.
[34] Kochanov RV, Gordon IE, Rothman LS, Wcisło P, Hill C, Wilzewski JS. HITRAN Application Programming Interface (HAPI): a comprehensive approach to working with spectroscopic data. J Quant Spectrosc Radiat Transfer 2016;177:15–30.
[35] Newville M., Otten R., Nelson A., Ingargiola A., Stensitzki T., Allan D., et al. Nonlinear least-squares minimization and curve-fitting for Python. 1.0.0 ed: 2019. 10.5281/zenodo.3588521.
[36] Liu AW, Hu CL, Wang J, Perevalov VI, Hu SM. Cavity ring-down spectroscopy of ^{15}N enriched N_2O near 1.56 μm. J Quant Spectrosc Radiat Transfer 2019;232:1–9.
[37] Song KF, Liu AW, Ni HY, Hu SM. Fourier-transform spectroscopy of $^{15}N^{14}N^{16}O$ in the 3500–9000cm^{-1} region. J Mol Spectrosc 2009;255:24–31.
[38] Ni HY, Song KF, Perevalov VI, Tashkun SA, Liu AW, Wang L, et al. Fourier–transform spectroscopy of $^{14}N^{15}N^{16}O$ in the 3800–9000cm^{-1} region and global modeling of its absorption spectrum. J Mol Spectrosc 2008;248:41–60.
[39] Hargreaves RJ, Gordon IE, Rothman LS, Tashkun SA, Perevalov VI, Lukashevskaya AA, et al. Spectroscopic line parameters of NO, NO_2, and N_2O for the HITEMP database. J Quant Spectrosc Radiat Transfer 2019;232:35–53.
[40] Ghysels M, Liu Q, Fleisher AJ, Hodges JT. A variable-temperature cavity ring–down spectrometer with application to line shape analysis of CO_2 spectra in the 1600nm region. Appl Phys B 2017:123.
[41] Hartmann J-M, Boulet C, Robert D. Collisional effects on molecular spectra: laboratory experiments and models, consequences for applications. Elsevier; 2008.
[42] Massman W. A review of the molecular diffusivities of H_2O, CO_2, CH_4, CO, O_3, SO_2, NH_3, N_2O, NO, and NO_2 in air, O_2 and N_2 near STP. Atmos Environ 1998;32:1111–27.
[43] Li H, Wilhelmsen Ø, Lv Y, Wang W, Yan J. Review of available experimental data and models for the transport properties of CO_2-mixtures relevant for CO_2 capture. Transp Storage 2021.
[44] Gamache RR, Roller C, Lopes E, Gordon IE, Rothman LS, Polyansky OL, et al. Total internal partition sums for 166 isotopologues of 51 molecules important in planetary atmospheres: application to HITRAN2016 and beyond. J Quant Spectrosc Radiat Transfer 2017;203:70–87.
[45] Fleurbaey H, Yi H, Adkins EM, Fleisher AJ, Hodges JT. Cavity ring-down spectroscopy of CO_2 near $\lambda = 2.06$ μm: accurate transition intensities for the Orbiting Carbon Observatory-2 (OCO-2) “strong band”. J Quant Spectrosc Radiat Transfer 2020;252:107104.
[46] Wilzewski JS, Birk M, Loos J, Wagner G. Temperature-dependence laws of absorption line shape parameters of the CO_2 ν_3 band. J Quant Spectrosc Radiat Transfer 2018;206:296–305.
[47] Kochanov VP. On parameterization of spectral line profiles including the speed-dependence in the case of gas mixtures. J Quant Spectrosc Radiat Transfer 2017;189:18–23.